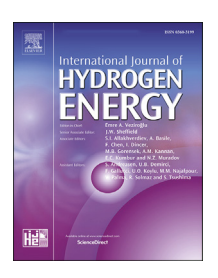


Available online at www.sciencedirect.com

ScienceDirect





Call attention to using DRT and EIS to quantify the contributions of solid oxide cell components to the total impedance



Yudong Wang a,b, Barbara Marchetti b, Xiao-Dong Zhou a,b,*

- ^a Department of Chemical Engineering, University of Louisiana at Lafayette, Lafayette, LA 70504, USA
- ^b Institute for Materials Research and Innovation, University of Louisiana at Lafayette, Lafayette, LA 70504, USA

HIGHLIGHTS

- Anode and cathode contributions to the impedance are investigated by DRT analysis.
- The impedance spectra are deconvoluted into five individual peaks in DRT domain.
- Systematic changes in the gas compositions allows quantifying the anode and cathode contributions to the impedance.
- Changing the buffer gas helps identifying the resistance arising from diffusion processes.
- Due to overlapping DRT peaks, attention should be paid while separating cathode and anode resistance.

ARTICLE INFO

Article history:
Received 2 March 2022
Received in revised form
11 July 2022
Accepted 10 August 2022
Available online 6 September 2022

ABSTRACT

The contributions of anode and cathode processes to solid oxide fuel cell (SOFC) impedance were studied using electrochemical impedance spectroscopy (EIS) and distribution of relaxation time (DRT). Specifically, the role of gas composition at both anode and cathode was explored in a systematic study aimed at deconvoluting, identifying and quantifying the contributions of different anode and cathode processes. Five distinct relaxation time distributions were observed in the DRT spectra; although the peaks were ascribed to diffusion and charge transfer processes at the electrodes, it was found that both electrodes contributed to various peaks at the same time. Moreover, it was found that two distinctive operating conditions could return equivalent DRT spectra. While DRT analysis allows to obtain useful information regarding cell performance, extra consideration is needed when assessing and quantifying anodic and cathodic resistances within the SOFC.

© 2022 Hydrogen Energy Publications LLC. Published by Elsevier Ltd. All rights reserved.

Introduction

Solid oxide fuel cells (SOFCs) are capable of generating electricity and simultaneously capturing CO_2 [1,2,4–7]. Furthermore, an important aspect which makes SOFCs particular attractive for practical applications is their capability of

operating reversely, by either generating power or producing hydrogen while using electricity, for instance, produced from renewable sources (electrolysis mode). Despite rapid advances in this field [1,8–10], optimization of the energy conversion efficiency and durability of cell materials still represents crucial aspects of SOFC design. Minimization of

^{*} Corresponding author. Department of Chemical Engineering, University of Louisiana at Lafayette, Lafayette, LA 70504, USA. E-mail addresses: ydwang1@louisiana.edu (Y. Wang), zhou@louisiana.edu (X.-D. Zhou). https://doi.org/10.1016/j.ijhydene.2022.08.093

electrode degradation processes during cell operation represents the first challenge in the design of SOFCs, as these devices are typically operated at high temperatures, at which degradation of the cell materials may be promoted, especially as a consequence of extensive or prolonged cell usage.

Most of the recent research efforts focus on evaluating the performance of a specific cell component, such as the cathode or the anode, by optimizing the electrode material composition and its intrinsic properties (e.g. thickness, porosity and conductivity) or experimental conditions (e.g. operating temperature), while keeping the remaining critical cell components unvaried. In this approach, improvement of cell performance is generally attributed exclusively to optimization in the specific property of the electrode material or experimental parameter. However, the controlled processes, which include gas diffusion, ionic transport and charge transfer reactions, may exhibit deviation from expected behaviour due to unavoidable experimental errors. Separation of the contributions of such processes occurring in different cell components is paramount to optimize cell performance since deep insights into the mechanisms which govern its operation are typically needed for this purpose.

Electrochemical impedance spectroscopy (EIS) is a widely used in-situ technique for SOFC performance evaluation [11–13]. A small AC perturbation is applied to the cell and the impedance of the cell versus AC frequency is recorded based on voltage respondence. The impedance spectrum provides abundant information about the reaction kinetics and transport process. The full cell impedance is consistent of three parts, the ohmic resistance (R_o), the charge transfer reaction impedances of cathode (Z_c) and anode (Z_a).

$$Z_{cell}(\omega) = Z_c(\omega) + R_o + Z_a(\omega)$$
 [1]

The high frequency intercept of the real axis in the Nyquist plot is ohmic resistance, R_{o} , which is considered to arise from the resistance of ionic transport in the electrolyte and independent of AC frequencies. The rest impedance provides useful information on different dynamic process in the electrodes.

Traditional EIS analysis is performed *via* the complex nonlinear least-squares fitting based on a provided equivalent

circuit model (ECM). The fitting result highly depends on the quality of the ECM used [14]. The downside of this approach is that the complete ECM requires a deep understanding and prior knowledge of the electrochemical system (and processes occurring within it) which are not available in many practical cases. By contrast, the distribution of relaxation time (DRT) approach represents a valid alternative which allows to investigate the system without any initial assumptions [15]. This approach can be used to directly convert the impedance spectra from the frequency domain to the relaxation time domain, by means of Eq. [2]

$$Z_{\text{cell}}(\omega) = R_o + \int_{-\infty}^{+\infty} \frac{\gamma}{1 + j\omega\tau} d(\ln\tau)$$
 [2]

where γ is distribution function of relaxation time, ω is the angular frequency and τ is the relaxation time. The transformed DRT spectrum has better resolution than the EIS, in that, it provides deeper insights into the nature of various processes which govern cell operation and aid unravelling the ways in which they depend on the operating conditions or materials characteristics [16,17]. For each relaxation time distribution appearing in the DRT spectra, the integrated area under the peak corresponds to the contribution to polarization resistance arising from the associated process. Schichlein et al. first applied this concept to the deconvolute their SOFC impedance spectra [18]. Since then DRT have been extensively used for identifying the ECM of the electrochemical system, leading to a detailed mechanistic interpretation of EIS results [19]. In recent years, DRT have been successfully used to investigate and advance the study and application of new materials for proton conductor fuel cells [20], oxygen-ion conducting solid oxide fuel cells (O-SOFC), and solid oxide electrolytic cells (SOEC), by enabling identification of crucial performance-determining processes, e.g. degradation mechanisms, Cr poisoning [21,22] and Sr segregation [23,24].

This work aims to investigate the feasibility of using EIS and DRT to deconvolute the cell impedance and to assign a peak to a specific electrode by systematically changing gas compositions in both electrodes in a full cell. Our results call attention to the use of DRT to differentiate distinct

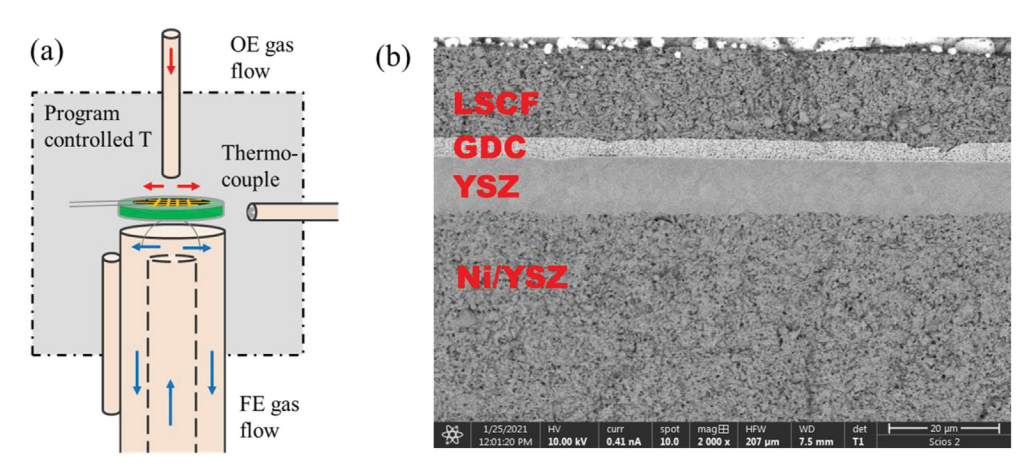


Fig. 1 - (a) Schematics of the electrochemical cell testing setup with controlled gas flows (b) SEM of the cross-section of the SOFC.

contributions arising from kinetics and diffusion processes occurring both at the cathode and anode, by systematically changing the gas compositions at both electrodes, including the nature of balance gas used. The experimental findings within this study suggest that, while DRT is a powerful tool for assessing the contributions of processes to the overall SOFC impedance, a more sophisticated analysis might be required for a deeper understanding of SOFC process mechanism.

Experimental methodology

The NiO/YSZ anode support tape and YSZ electrolyte tape are fabricated from tape casting process. The two tapes are laminated together and sintered at 1375 °C to obtain a bilayer. A layer of gadolinium doped ceria, $Gd_{0.2}Ce_{0.8}O_{1.9}$ (GDC), was screen-printed onto the electrolyte, following by sintering at 1200 °C for 2 h. The thickness of this barrier layer is about 5 μ m. The La_{0.6}Sr_{0.4}Co_{0.2}Fe_{0.8}O₃ (LSCF) layer of 2 cm² was screen printed on the GDC to form a porous cathode of about 30 μ m in thickness, after sintering at 1080 °C for 30 min. The gold grid is also fabricated by screen printing on the LSCF layer as the cathode current collector. A nickel mesh is attached to the anode support with NiO ink. The current collectors are sintered at 900 °C for 30 min. The microstructure of the SOFC cross-section is imaged with scanning electron microscope (SEM, ThermoFisher Scios 2), which is shown in Fig. 1b.

The full cell was electrically connected to a four-probe setup, shown in Fig. 1a. Each gas flow is controlled with a mass flow controller before mixing. The mixed anode gas passes through a bubbler filled with DI water at room temperature to provide 3% humidity to the anode. The anode chamber and the bubbler are purged with pure nitrogen gas and the anode support is reduced with H₂/N₂ mixture at 750 °C for 2 h. The linear sweep voltammetry is performed to obtain IV curve with a scanning rate of 5 mV/s with the electrochemical station VMP3 (Bio-Logic). The impedance spectra were evaluated with an alternative current perturbation amplitude of 20 mA from 50 kHz to 0.1 Hz. Distribution of relaxation time analysis is performed by the DRTTools with a regularization parameter of 0.001 [15]. The areas of peaks are calculated by fitting the DRT spectrum with the gaussian functions and integrating the corresponding areas beneath the function.

Results and discussion

Theoretical analysis

For the charge transfer reaction that follows a Butler-Volmer type kinetics, at the cathode side, ORR and OER occurs (though it contains multiple elemental reactions at the active sites),

$$\frac{1}{2}O_2(g) + V_0^{\cdot \cdot}(LSCF) \rightleftharpoons O_0^{\times}(LSCF) + 2h^{\cdot}(LSCF)$$
 [3]

The current density, i, can be expressed as:

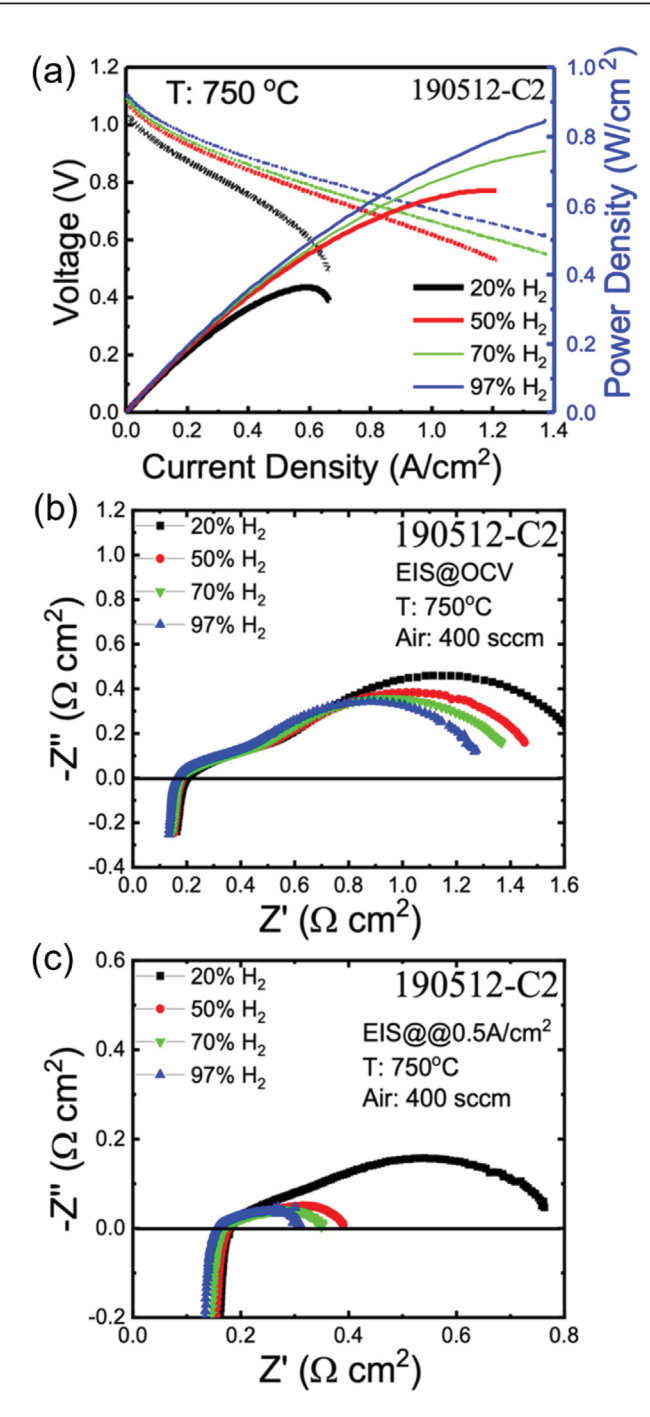


Fig. 2 – (a) IV curve and power density plot for the Ni-based anode at various H_2 in N_2 carrier gas (3% humidity), i.e. 97% H_2 (blue), 70% H_2 (green), 50% H_2 (red) and 20% H_2 (black). The curves were recorded at 750 °C. A steady decline in the cell performance is observed as the partial pressure of H_2 in fuel gas mixture is decreased. (b) EIS@OCV, and (c) EIS@0.5A/cm² under various anode gas compositions (20% H_2 , 50% H_2 , 70% H_2 and 97% H_2 , balanced by 3% H_2 O and N_2). The ESI spectra exhibit a marked dependence on the composition of the humidified H_2/N_2 fuel mixture. (For interpretation of the references to colour in this figure legend, the reader is referred to the Web version of this article.)

Table 1 — Dependence of P1 — P5 on the gas composition. The table reports the relative percentage changes calculated with reference to the values at $97\% H_2$ for the anode, and $100\% O_2$ for the cathode.									ated with		
			Anode at O	CV			And	ode at 0.5 A	cm ⁻²		
H ₂ %	P1	P2	Р3	P4	P5	P1	P2	P3	P4	P5	
70	19.9	6.7	4.1	-2.2	2.5	16.0	-7.0	21.2	-11.2	40.3	
50	25.2	20.2	5.7	-6.7	19.8	11.6	6.0	37.6	-7.5	153.9	
20	30.6	49.0	-1.8	-24.4	52.6	2.5	43.6	127.2	293.3	1131.5	
Cathode at OCV						Cathode at 0.5 A cm ⁻²					
O ₂ %	P1	P2	Р3	P4	P5	P1	P2	Р3	P4	P5	
80	0.8	7.9	5.4	-1.3	13.8	-3.1	-3.0	10.1	-5.7	41.9	
60	1.8	11.5	17.0	-2.0	27.2	-3.9	-6.3	17.9	-3.3	18.0	
40	0.0	29.5	19.6	-1.2	54.1	-9.2	-9.2	16.1	-2.7	39.9	
20	-0.8	52.3	23.6	-1.4	115.6	-7.4	-11.3	27.0	5.0	112.2	
10					167.2	-12.9	-13.3	58.6	-5.6	213.7	

$$i = i_{0,c} exp(b_{OER} \eta_c) - i_{0,c} \left(\frac{C_{O_2}}{C_{O_2,0}}\right)^l exp(-b_{ORR} \eta_c) + C_c \frac{d\eta_c}{dt} \eqno{[4]}$$

where $i_{0,c}$ is the exchange current density of the cathode, l is the order of reaction respective to oxygen, C_{O_2} is the oxygen concentration at the triple phase boundary, $C_{O_2,0}$ is the reference concentration, η_c is the overpotential of the electrode, b_{OER} and b_{ORR} are Tafel slope of OER and ORR respectively, and C_{c} is the area specific capacitance. By introducing a sinus wave perturbation, $\tilde{i} = \delta i \exp(j\omega t)$, to the system, we can write:

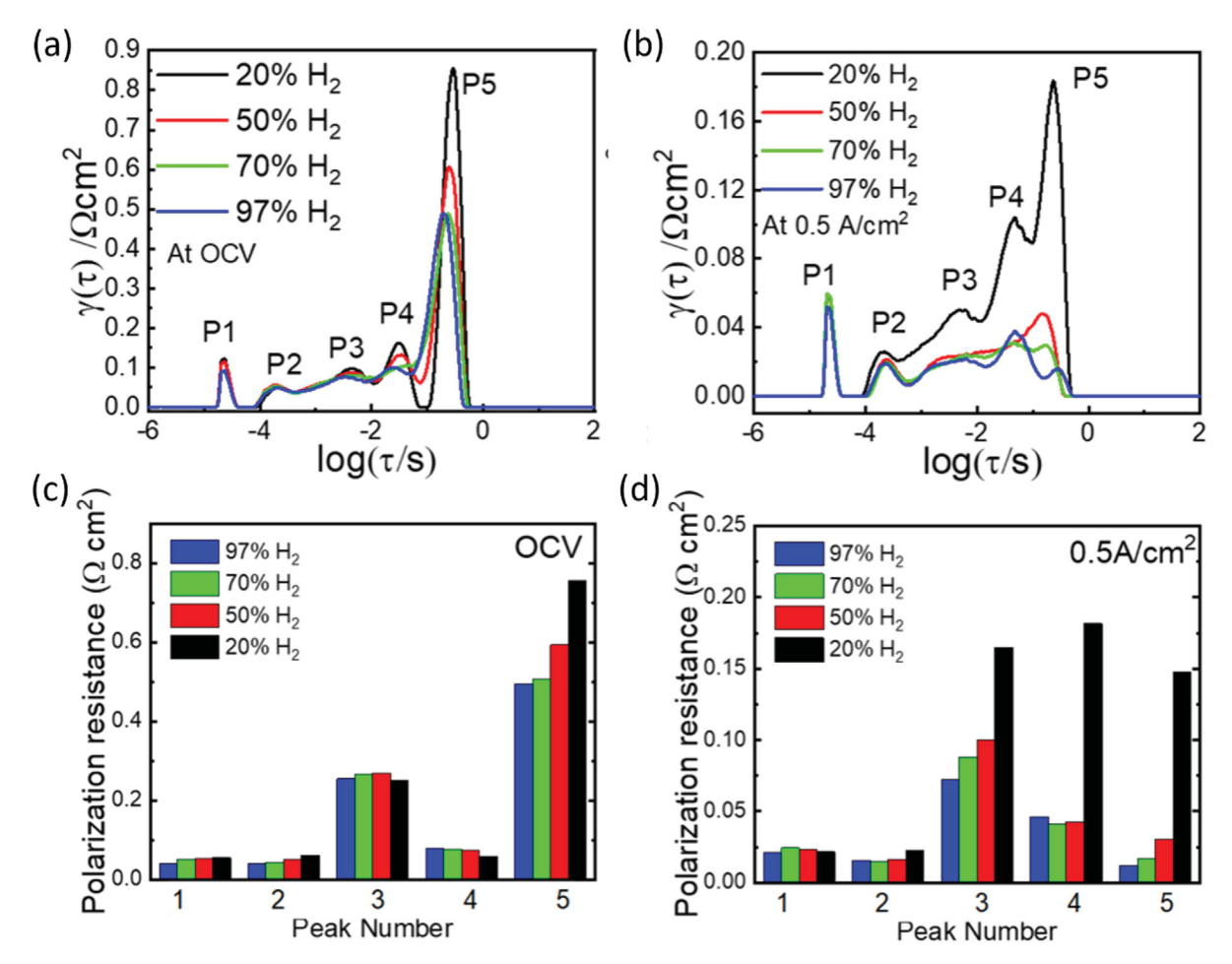


Fig. 3 – DRT analysis of the peaks vs H₂ concentration at (a) OCV and (b) 0.5 A cm⁻². Five peaks are observed in the spectra. The various gas mixtures contained, 20% H₂ (black line), 50% H₂ red line, 70% H₂ (green), 97% H₂ (blue). The polarization resistance of each peak as a function of the percentage fraction of H2 in the DRT spectra is reported at (c) OCV and (d) 0.5 A cm^{-2} .

$$\begin{split} \widetilde{i} &= i_{0,c} \left[b_{\text{OER}} \exp(b_{\text{OER}} \eta_{\text{OE}}) + b_{\text{ORR}} \left(\frac{C_{\text{O}_2}}{C_{\text{O}_2,0}} \right)^l \exp(-b_{\text{ORR}} \eta_c) \right] \widetilde{\eta_c} \\ &- \frac{li_{0,c}}{C_{\text{O}_2,0}} \left(\frac{C_{\text{O}_2}}{C_{\text{O}_2,0}} \right)^{l-1} \exp(-b_{\text{ORR}} \eta_c) \widetilde{C_{\text{O}_2}} + j\omega C_c \widetilde{\eta_c} \end{split}$$
[5]

where ω is the angular frequency of the sinus wave. Here we define the OER (R_{OER}), ORR (R_{ORR}) and total charge transfer resistance (R_{ctc}) in the cathode:

$$R_{OER} = [i_{0,c}b_{OER} \exp(b_{OER}\eta_c)]^{-1}$$
 [6]

$$R_{ORR} = \left[i_{0,c} \left(\frac{C_{O_2}}{C_{O_2,0}}\right)^l b_{ORR} \exp(-b_{ORR}\eta_c)\right]^{-1}$$
 [7]

$$R_{\text{ct,c}} = \left(R_{\text{OER}}^{-1} + R_{\text{ORR}}^{-1}\right)^{-1}$$
 [8]

On can easily obtain

$$Z_{c}(\omega) = \frac{\widetilde{\eta_{c}}}{\tilde{i}} = \frac{\left[R_{ct,c} + \frac{R_{ct,c}\frac{i_{0,c}}{C_{0_{2},0}}\left(\frac{c_{0_{2}}}{c_{0_{2},0}}\right)^{l-1}\exp(-b_{ORR}\eta_{c})\widetilde{C_{0_{2}}}}{\tilde{i}}\right]}{1 + j\omega C_{c}R_{ct,c}} = \frac{R_{ct,c} + Z_{D,O_{2}}}{1 + j\omega C_{c}R_{ct,c}}$$
[9]

where Z_{D,O_2} is the oxygen diffusion impedance [25]:

$$Z_{D,O_2} = R_{ct,c} \frac{li_{0,c}}{4FD_{O_2,\;X}C_{O_2,0}} \left(\frac{C_{O_2}}{C_{O_2,0}}\right)^{l-1} exp(-b_{ORR}\eta_{OE}) \frac{-\widetilde{C_{O_2}}}{\frac{d\widetilde{C_{O_2}}}{dy}\big|_{TPB}}$$
[10]

 $D_{O_2,\;X}$ is the binary diffusion coefficient with the balance gas, X. $D_{O_2,\;X}$ decreases with the molecular weight of the balanced gas, which will result in a rise in Z_{D,O_2} . For the anode one can also write:

$$Z_{a}(\omega) = \frac{R_{\text{ct},a} + Z_{\text{D,H}_{2}O} + Z_{\text{D,H}_{2}}}{1 + j\omega C_{a}R_{\text{ct},a}}$$
[11]

where $R_{ct,\alpha}$ considers the contribution from both hydrogen evolution reaction (HER) and hydrogen oxidation reaction (HOR).

$$2e'(Ni) + H_2O(g) + V_O^{\cdot \cdot}(YSZ) \stackrel{\sim}{\rightleftharpoons} O_O^{\times}(YSZ) + H_2(g)$$
 [12]

$$R_{\text{HER}} = \left[i_{0,a} b_{\text{HER}} \left(\frac{C_{\text{H}_2\text{O}}}{C_{\text{H}_2\text{O},0}} \right)^n \exp(-b_{\text{HER}} \eta_a) \right]^{-1}$$
 [13]

$$R_{HOR} = \left[i_{0,a}b_{HOR}\left(\frac{C_{H_2}}{C_{H_{0},0}}\right)^m \exp(b_{HOR}\eta_a)\right]^{-1}$$
 [14]

$$R_{\text{ct},a} = \left(R_{\text{HOR}}^{-1} + R_{\text{HER}}^{-1}\right)^{-1}$$
 [15]

The total impedance consists of basically six components including ohmic resistance, charge transfer reactions in the cathode ($R_{ct,c}$), oxygen diffusion (Z_{D,O_2}), charge transfer reactions in the anode ($R_{ct,a}$), steam diffusion (Z_{D,H_2O}) and hydrogen diffusion (Z_{D,H_2}).

$$Z_{cell}(\omega) = R_o + \frac{R_{ct,c} + Z_{D,O_2}}{1 + j\omega C_c R_{ct,c}} + \frac{R_{ct,a} + Z_{D,H_2O} + Z_{D,H_2}}{1 + j\omega C_a R_{ct,c}}$$
[16]

The ohmic resistance can be separated from high frequency intercept. The other five components do have an

imaginary component and each of them has a specific distribution of relaxation time. As a result, if the relaxation time distribution for two components is the same, these two components may not be differentiated from this analysis.

The experimental results

Effect of anode gas composition on the EIS and DRT analysis DC current-voltage (IV) and EIS measurements were acquired by tuning the partial pressure of H_2 (P_{H2}) in the H_2/N_2 fuel

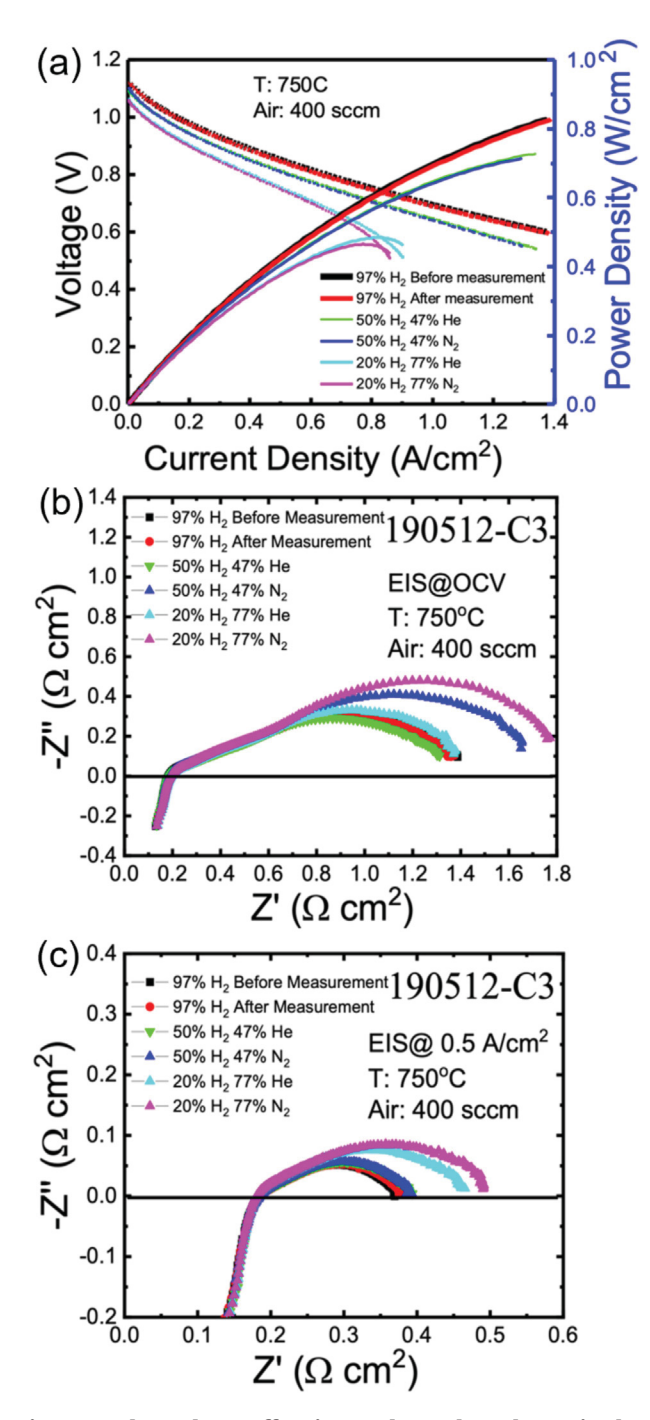


Fig. 4 – Balanced gas effect in anode, replace the $\rm N_2$ in the anode with He. (a) IV, (b) EIS@OCV, and (c) EIS@0.5A cm $^{-2}$ vs anode gas composition.

mixture. Different $P_{\rm H2}$ values result in changes in the anode kinetics and the variety of anode impedance. In the IV curves in Fig. 2a, the voltage drops as a function of the current density; the associated gradient become progressively steeper as $P_{\rm H2}$ is decreased, indicating higher resistance, thus decreased cell performance, as H_2 is depleted at the triple phase boundary. This may imply a performance limiting factor for the operation of the SOFC, particularly at critically low $P_{\rm H2}$ (e.g., at 20% H_2).

Fig. 2b and c display the EIS acquired at open-circuit voltage (OCV) conditions (\sim 1.1 V) and 0.5 A cm⁻² (\sim 0.9-0.7 V). The EIS curves feature at least two distinct but overlapping arcs. The most prominent arc is observed at low frequencies, while the second feature, arising at high

frequencies, intercepts the real impendence axis at ~0.180 Ω cm² (ohmic resistance). The curves in Figure 2b and c illustrate that the use of higher P_{H2} leads to lower ohmic and polarization resistance, thus overall improvement in the SOFC performance.

The combination of IV and EIS measurements offers valuable, but rather generic insights into the loss processes, which may limit cell performance. The intrinsic limitation of such techniques is their inability to provide process-specific information; here, the use of DRT approach provides a viable way of disentangling such coupled processes. Fig. 3a and b report the DRT spectra acquired at various $P_{\rm H2}$ at OCV and 0.5 A cm⁻², respectively. The spectra exhibit at least five distinct, although overlapping distributions (henceforth P1 –

reference to the values at 97% H_2 for the anode, and 100% O_2 for the cathode.										
		A	node at OC	V			Ano	de at 0.5 A c	m^{-2}	
% buffer	P1	P2	Р3	P4	P5	P1	P2	Р3	P4	P5
47% He	2.7	-13.0	-4.3	-8.7	12.8	-10.5	3.3	2.6	10.9	11.5
77% He	6.1	-29.7	2.7	-12.6	55.0	-26.0	24.4	63.8	44.0	118.7
47% N ₂	0.5	0.6	21.8	16.5	80.4	-10.8	-4.9	7.1	15.9	33.1
77% N ₂	3.0	-8.1	16.7	21.7	78.1	-27.4	20.1	113.2	44.5	195.3
Cathode at OCV							Catl	node at 0.5 A c	m^{-2}	
% buffer	P1	P2	Р3	P4	P5	P1	P2	Р3	P4	P5
40% He	_2 1	_15.5	24.1	12.5	23.5	_0.9	_23	_25.3	23.4	_12.0

Table 2 - Dependence of P1 - P5 on the buffer gas. The table reports the relative percentage changes calculated with

		Ca	thode at OC	V			Cath	ode at 0.5 A ci	m -	
% buffer	P1	P2	P3	P4	P5	P1	P2	P3	P4	P5
40% He	-2.1	-15.5	24.1	18.5	23.5	-0.9	-2.3	-25.3	23.4	-12.0
80% He	-5.5	-17.6	87.3	38.8	33.5	-1.9	-22.0	-44.4	71.2	-16.8
90% He	-8.3	-12.0	85.9	49.5	70.1	-3.0	-10.4	-62.6	91.1	75.4
40% N ₂	-2.6	-29.8	37.9	16.1	42.0	-0.2	-10.3	-16.8	26.5	-8.1
80% N ₂	-8.1	-28.9	98.2	52.1	63.6	-4.2	-15.7	-57.8	85.9	21.6
90% N ₂	-11.9	-25.0	99.6	64.1	90.0	-3.9	-30.7	-52.5	90.0	325.1

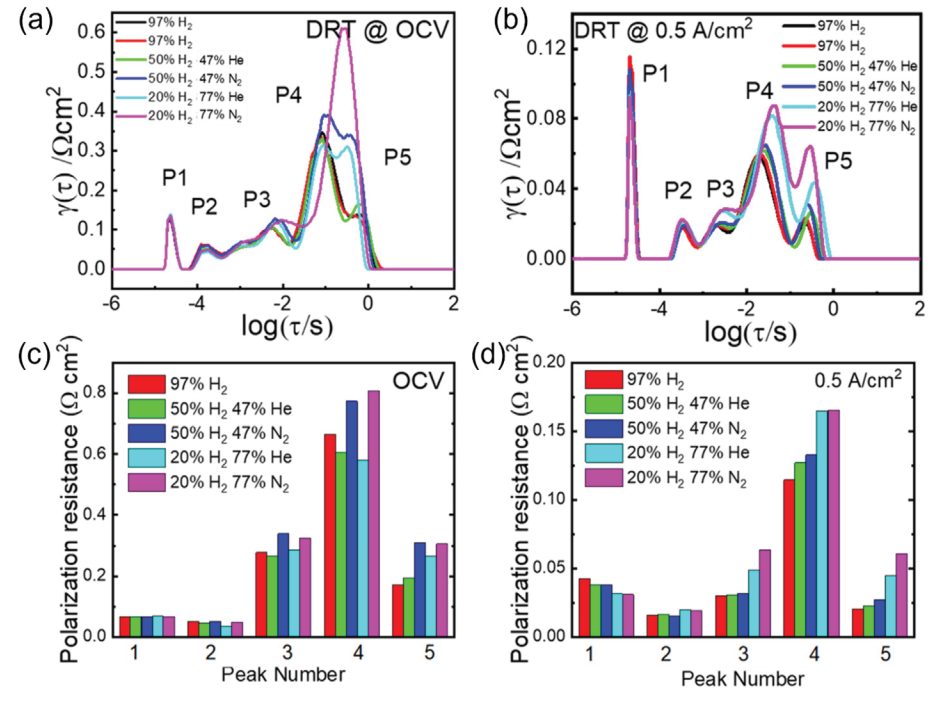


Fig. 5 – DRT analysis of EIS at (a) OCV and (b) $0.5A \text{ cm}^{-2}$ with helium or nitrogen as balanced gas. The polarization resistance of each peak as a function of the percentage fraction of H_2 and nature of balanced gas (N_2 vs He) in the DRT spectra is reported at (c) OCV and (d) 0.5 A cm^{-2} .

P5, from high frequency to low frequency), which can be attributed to various physical and chemical processes with different relaxation times contributing to the SOFC polarization resistance. P1 is a sharp high frequency peak at about 50 kHz. P2 locates from 1 kHz to 10 kHz, which merges with a broad P3 (20Hz-2000 Hz). P4 and P5 are both low frequency peaks (0.2 Hz-100 Hz) and contributes the most resistance at OCV. By changing P_{H2} value in the anode, the polarization resistance associated with each peak at different PH2 is displayed the bar charts in Fig. 3c and d, while Table 1 shows the relative percentage changes at various PH2, with reference to the measurement at 97% H₂ (v. Table S1 for absolute values). The distribution P5 provides the largest contribution to the overall polarization resistance which increases with decreasing P_{H2} and it depends more markedly on P_{H2} cf. P1 – P4. While P5 dominates the DRT spectra, the distributions are considerably overlapped, making it challenging to deconvolute the individual peak contributions.

Analogous measurements were carried out in two the carrier gases, namely N_2 and He, at 50% and 20% H_2 (Fig. 4). While the IV measurements (Fig. 4a) show no substantial difference between the two gases, the low frequency arc in the EIS spectra show some dependence, more evidently at OCV conditions (Fig. 4b), wherein the use of He yields to overall lower polarization resistance. By contrast, the P_{H2} appears the dominant limiting factor at 0.5 A cm $^{-2}$. The corresponding DRT spectra and associated analysis are reported in Fig. 5a–d, with absolute values and percentage changes in Table S2 and Table 2. Again, the use of He leads to overall lower resistance of N_2 , especially with reference to P4 and P5.

The effect of cathode gas composition on the EIS and DRT analysis

The IV and EIS measurements were acquired at 750 $^{\circ}$ C while tuning the percentage fraction of O₂ (P_{O2}) between 10% and 100%, with the fuel composition fixed at 97% H₂ (3% H₂O) at the anode. High P_{O2} induces faster cathode kinetics and lower cathode resistance.

As for the anode, the IV traces in Fig. 6a show a progressively steeper gradient as $P_{\rm O2}$ decreases, implying that high $P_{\rm O2}$ is a determining factor for optimal cell operation. The EIS spectra in Fig. 6b and c display multiple, convoluted arcs. Here, the ohmic resistance is independent of $P_{\rm O2}$. However, the polarization resistance varies considerably at different gas compositions, with the lowest resistance found at 100% O_2 .

The corresponding DRT spectra are reported in Fig. 7a and b with the associated analysis displayed in panels c and d. Relative percentage changes in the polarization resistance for P1 – P5 are displayed in Table 1 (relative to 100% O_2) while the absolute values can be found in Table S3. Again, P5 is the most heavily affected by changes in the gas composition, with lower contributions at high P_{O2} . At OCV, both P2 and P3 show similar although less pronounced trends cf. P5, while P2 and P4 seem less affected by the gas composition.

Effect of the buffer gas in cathode (N_2 and He) is reported in Figs. 8 and 9. The IV curves (Fig. 8a) show the same trends for both gases; however, the use of He returns lower resistance at low P_{O2} . The observation is consistent with the EIS spectra (Fig. 8b and c), wherein the polarization resistance in He is lower. By analysis of the DRT spectra (Fig. 9 a - d, Table S4 and

Table 2), it is deduced that some dependence on the balance gas may be observed for P4 and P5.

General discussion

The DRT analysis at OCV

The DRT analysis performed above relies on tuning the gas composition at each electrode to assess its contributions to the SOFC impedance. This approach relies on the assumption that peaks are sufficiently decoupled and resolved, so as to allow to identify the processes occurring at each electrode by using appropriate changes in the corresponding gas

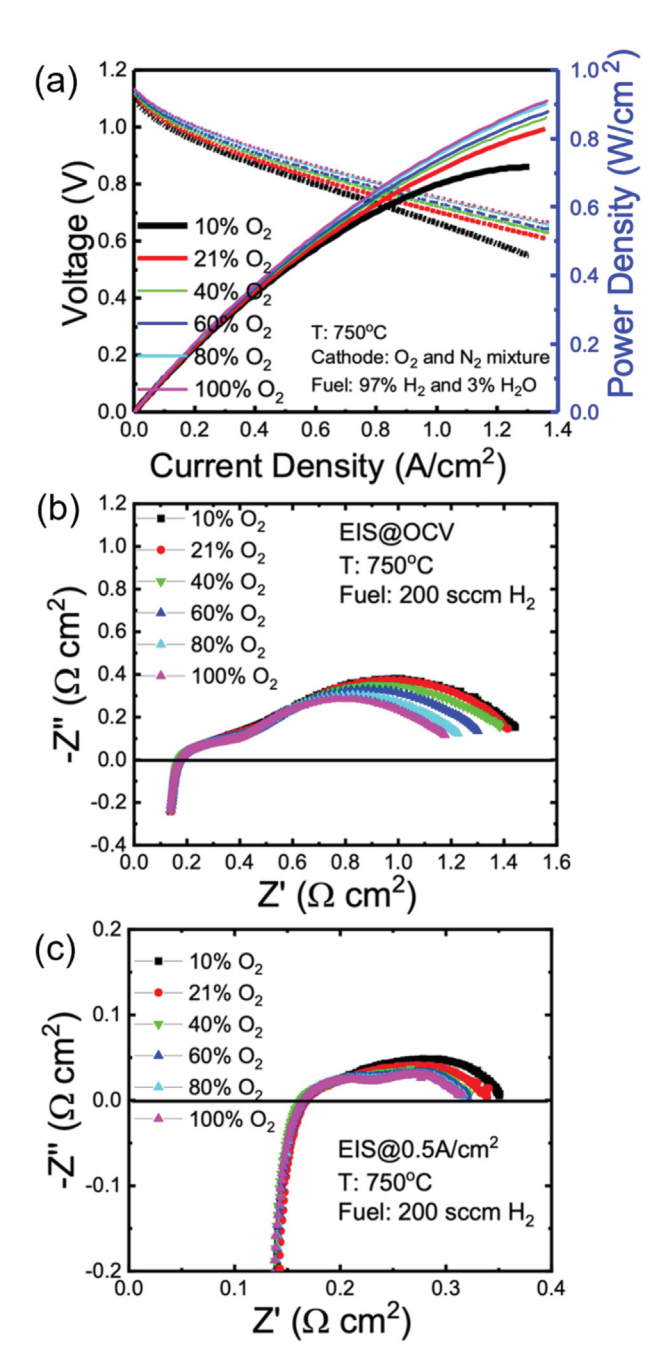


Fig. 6 – IV, EIS@OCV, and EIS@0.5A/cm2 vs cathode gas composition (10% O_2 , 21% O_2 , 60% O_2 and 100% O_2 , balanced by N_2).

composition. In reality, as also observed in this study, multiple peaks in the DRT spectra may embed considerable contributions of both anode and cathode. In these circumstances, separation and quantification of cathode and anode contributions might be challenging.

For instance, in Fig. 7, we differentiate the cathode process in DRT based on the response of peaks on oxygen partial pressure. The cathode material, LSCF, is a mixed ionic and electronic conductor and higher $P_{\rm O2}$ value results in the oxidation of B site ions to create more electronic defects and higher electronic conductivity [26]. In addition, the oxygen ion transport is sluggish with the reduction in oxygen vacancy concentrations due to high $P_{\rm O2}$ [27], which shows the increase in P1. Comparison with similar studies in recent literature may suggest that this peak arises from to ionic conduction and/or charge transfer processes [28–30]. The electrochemical reactions, OER and ORR, are also affected by oxygen concentrations, which contributed with significant cathode impedance. Under open circuit condition, the overpotential equals 0,

$$R_{\text{ct,c}} = \left[i_{0,c} b_{\text{OER}} + i_{0,c} \left(\frac{C_{O_2}}{C_{O_2,0}} \right)^l b_{\text{ORR}} \right]^{-1}$$
 [17]

The resistance, $R_{\text{ct.c}}$, comes from the parallel relation between OER and ORR. Under most cases, ORR kinetics is faster due to its lower Tafel slope and higher oxygen concentration

leads to lower $R_{ct,c}$. In addition, the impedance arises from the oxygen diffusion, Z_{D,O_2} , is proportional to $R_{ct,c}$ (Eq. [10]). Therefore, Fig. 7 indicates P3 to P5 have a clear response to changes P_{O2} , suggesting that also a substantial cathodic resistance may arise in correspondence of P3 to P5 as the low P_{O2} . To further differentiate the gas diffusion, oxygen is balanced by two inert gases (N_2 and He) The light He balance gas results in higher binary diffusion coefficient [31], which leads to lower Z_{D,O_2} values. By only changing the diffusion coefficient, the resistance contribution from cathode gas diffusion can be identified. When considering Fig. 9, different buffer gas with same P_{O2} at the cathode largely affects P5, indicating P5 is governed by oxygen diffusion in the electrode.

In Fig. 3, the decreases of $P_{\rm H2}$ results in the drop of cell impedance. At open circuit condition, the overpotential equals 0 and the resistance due to the electrochemical reaction in anode ($R_{\rm ct,a}$) can be written as

$$R_{ct,a} = \left(i_{0,a}b_{HER}\left(\frac{C_{H_2O}}{C_{H_2O,0}}\right)^n + i_{0,a}b_{HOR}\left(\frac{C_{H_2}}{C_{H_2,0}}\right)^m\right)^{-1}$$
[18]

All the reactions are reversible under OCV and their kinetics contributes to the anode exchange current density. Lower P_{H2} indicates lower C_{H2} and therefore higher $R_{ct,a}$. In addition, higher $R_{ct,a}$ leads to higher Z_{D,H_2O} and Z_{D,H_2} values. Thus, DRT spectrum changes in P3, P4 and P5 (Fig. 3) can be ascribed to resistance arising from the anode processes

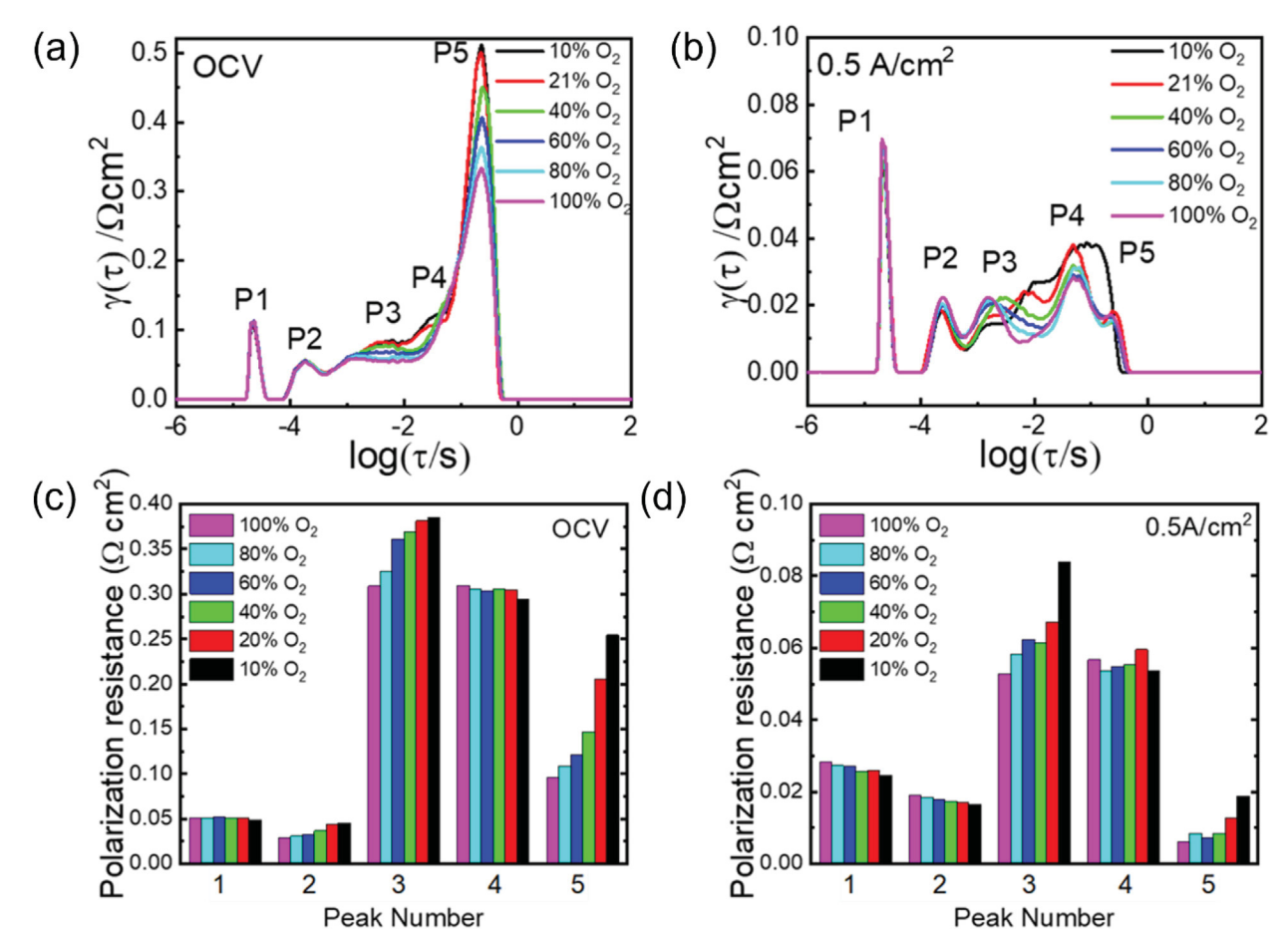


Fig. 7 – DRT analysis of the peaks vs O_2 concentration. @OCV and @0.5A cm⁻².

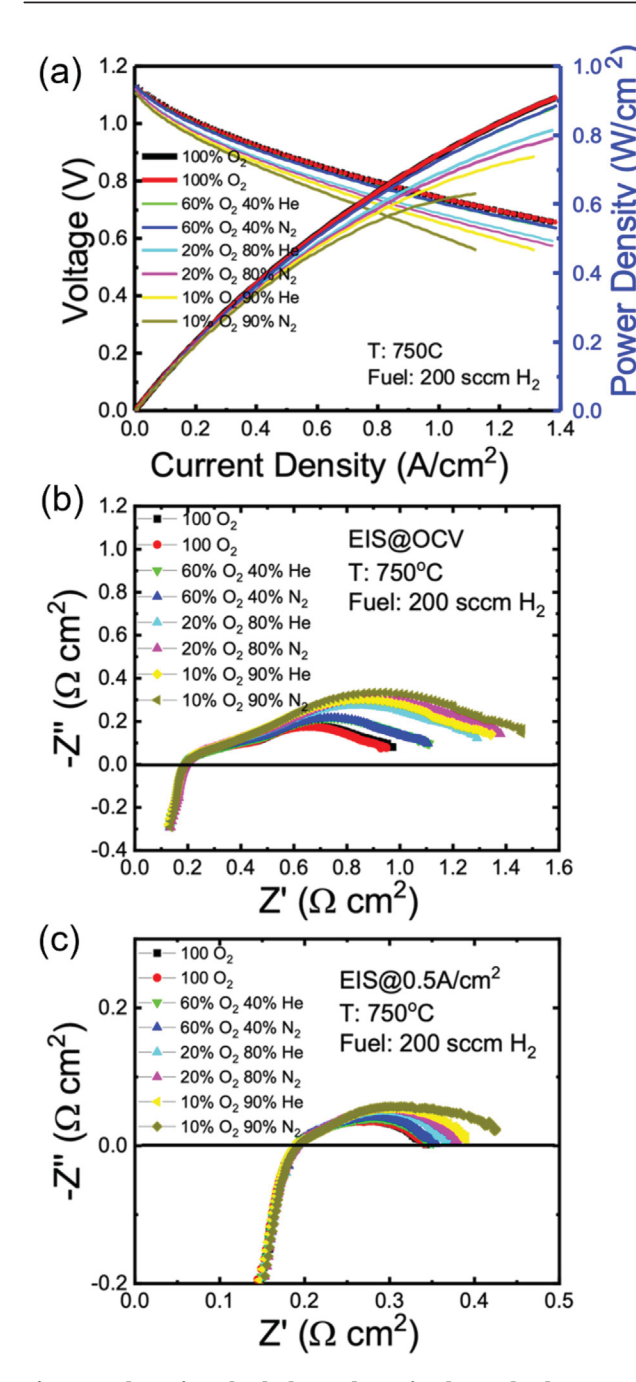


Fig. 8 – Changing the balanced gas in the cathode atmosphere on the IV and EIS of the fuel cell.

related to reactions and gas diffusion. Analogy to the cathode diffusion process study, P4 and P5 show significant response to the balance gas in anode, which is agreement with previous studies performed on SOFC assemblies, which attribute a low frequency peak (1–10 Hz) to the diffusion of fuel gas mixture at the anode [16,28,29,32].

One may notice that P5 contributes the most to the impedance at OCV condition and represents both cathode and anode gas diffusion processes. Furthermore, P3 – P4 are also dependent on both PH2 and PO2, suggesting, again, both cathodic and anodic resistances are embedded into these peaks, making it challenging to deconvolute the contribution of each electrode. In accord with previous literature [29], these trends for P3 and P4 suggest that these contributions to polarization resistance arise from electrochemical or charge transfer processes. Oxygen ion transport in the anode also contributes significantly to the impedance; such contribution is determined by the conductivity of the YSZ phase in the composite anode. The concentration of charge carrier, oxygen vacancy, can hardly change with PH2 variation in the range 0.2-0.97 atm. P2 keeps almost a consistent shape by changing either P_{H2} and P_{O2} value at OCV, and it locates at high frequency (1 kHz-10 kHz) and represent ion transport process in the anode. The position and processes of all peaks are summarized in Table 3.

Finally, an additional consideration should be made when analysing DRT spectra with the purpose of assessing anode and cathode contributions to the SOFC impedance. The DRT analysis is generally considered a valid approach to investigate the physical and chemical processes contributing to the SOFC impedance without any a priori knowledge or initial assumptions. However, the single DRT spectra, taken alone, do not carry any intrinsic information about such processes; only through systematic studies, wherein a single parameter (temperature, gas composition, current density etc) is judiciously varied at once, it is possible to obtain insights into the SOFC mechanisms and their contribution to the impedance [33]. The presence of multiple variables which can affect and determine cathodic and anodic resistances makes separating electrode contributions challenging. For instance, Fig. 10 shows two DRT spectra which are acquired under different conditions; the spectra suggest that different operating conditions can lead to equivalent DRT spectra. In this case, by changing both $P_{\rm O2}$ and PH2, similar spectral pattern can be obtained. Two or more variables make the deconvolution problems more complex and require more attention on the separation of anode and cathode impedance. Though DRT analysis itself does not depend on the

Table 3 — Summary of all peaks with their corresponding frequencies and processes.							
Peaks	Frequency Range	Process					
P1	~50 kHz	Ion transport in cathode.					
P2	1 kHz–10 kHz	Ion transport in anode					
P3	20Hz to 2000 Hz	Cathode and anode electrochemical reactions (charge transfer)					
P4	10 Hz-100 Hz	Cathode and anode electrochemical reactions (charge transfer) and anode gas diffusion					
P5	0.2 Hz-20 Hz	Cathode gas diffusion and anode gas diffusion					

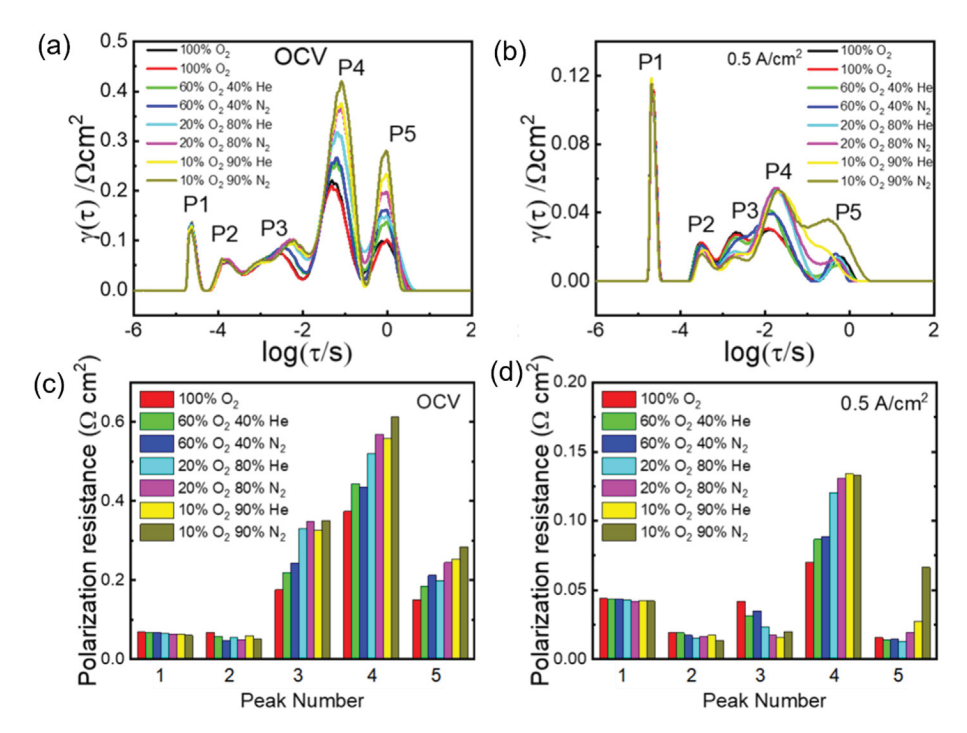


Fig. 9 – DRT analysis of EIS at OCV and 0.5A cm⁻² with different O₂ concentration and balanced gas.

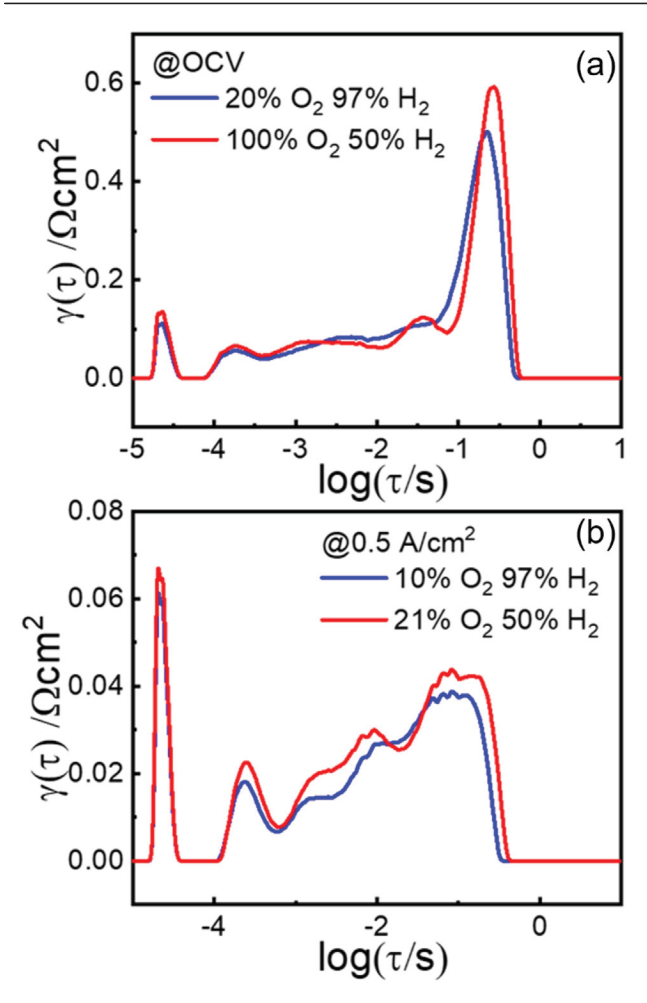


Fig. 10 – Similar DRT spectrums under different conditions at (a) OCV and (b) $0.5A~{\rm cm}^{-2}$.

physical process, a better deconvolution process should be based on more reasonable fitting functions relying on a better understanding of the process mechanisms.

The DRT analysis at 0.5 A cm^{-2}

The effect of current density was explored in each set of measurements, as this parameter can have a great impact in the resulting spectra. The EIS measurements at 0.5 A cm $^{-2}$ (Figs. 2c and 4c) show that, while the ohmic resistance remain relatively unaffected, the impedance arcs become considerably less prominent cf. the equivalent measurements at OCV, which suggests overall lower polarization resistance. The charge transfer resistances for cathode and anode are reduced significantly due to the exponential term ($\eta_{\rm c}$ <0 and η_a >0) in Butler-Volmer equation.

$$R_{ct,c} = \left[i_{0,c} b_{ORR} \left(\frac{C_{O_2}}{C_{O_2,0}} \right)^{l} \exp(-b_{ORR} \eta_c) \right]^{-1}$$
 [19]

$$R_{\text{ct},a} = \left[i_{0,a} b_{\text{HOR}} \left(\frac{C_{\text{H}_2}}{C_{\text{H}_2,0}} \right)^m \exp(b_{\text{HOR}} \eta_a) \right]^{-1}$$
 [20]

As diffusion impedances are associated with the charge transfer resistances, their values also decrease. More specific information regarding the impact of current density on cathodic and anodic resistances can be obtained through DRT analysis. In terms of absolute values, if one considers the equivalent measurements at 97% $\rm H_2$ and 100% $\rm O_2$ in Figs. 3b and 5b, the decrease in polarization resistance is largely associated with P3 – P5, while the resistance associated with P1 and P2 appear less affected. Furthermore, a more pronounced dependence on the $\rm P_{H2}$ and $\rm P_{O2}$ cf. OCV is observed, especially for P5 (Table 1, S1 and S2). The distribution P3 also seems to increase more sharply with decreased $\rm P_{H2}$ and $\rm P_{O2}$ cf. OCV conditions.

Other processes may exhibit different dependence on either or both P_{H2} and P_{O2} cf. OCV conditions. For instance, P1 and P2 are now shown to decrease at lower P_{O2} .

In general, the results indicate that while current density leads to overall lower SOFC resistance, gas diffusion resistance appears to be heavily impacted by the current density, with the anodic contribution to the SOFC being considerably reduced, while a weaker effect of current density is observed for other peaks, such as those associated with charge transfer processes.

Conclusions

Systematic electrochemical studies were performed to evaluate the contributions of cathode and anode to the overall resistance of the SOFC. IV and EIS measurements were first undertaken to evaluate the overall cell resistance. DRT analysis allowed obtaining process-specific information regarding losses occurring during operation of the cell. The analysis allowed deconvoluting and quantifying contributions to the resistance of processes occurring at the anode and cathode and their dependence on operating conditions, such as concentration of reactants or nature of the carrier gas. Judging from the DRT spectra, five peaks were observed in an SOFC, which are attributed to the charge and mass transfer in electrodes and across the interfaces. While it is natural to assign a specific peak to an electrode, this work shows that both electrodes may contribute to various peak at the same time. More importantly, it is possible that two distinctive operations may exhibit a similar DRT spectrum. While DRT analysis is indeed very powerful, extra attention is needed when using it to assign a peak to a specific electrode process.

Declaration of competing interest

The authors declare that they have no known competing financial interests or personal relationships that could have appeared to influence the work reported in this paper.

Acknowledgments

The authors would like to thank the US Department of Energy for the supports under DE-FE0031667 and DE-EE0009421.

Appendix A. Supplementary data

Supplementary data to this article can be found online at https://doi.org/10.1016/j.ijhydene.2022.08.093.

REFERENCES

- [1] Hussain S, Yangping L. Review of solid oxide fuel cell materials: cathode, anode, and electrolyte. Energy Transitions 2020;4:113–26.
- [2] Wilson JR, Kobsiriphat W, Mendoza R, Chen H-Y, Hiller JM, Miller DJ, Thornton K, Voorhees PW, Adler SB, Barnett SA.

- Three-dimensional reconstruction of a solid-oxide fuel-cell anode. Nat Mater 2006;5:541–4.
- [4] Bessler WG, Vogler M, Störmer H, Gerthsen D, Utz A, Weber A, Ivers-Tiffée E. Model anodes and anode models for understanding the mechanism of hydrogen oxidation in solid oxide fuel cells. Phys Chem Chem Phys 2010;12:13888–903.
- [5] Lohmann FP, Schulze PSC, Wagner M, Naumov O, Lotnyk A, Abel B, Varga Á. The next generation solid acid fuel cell electrodes: stable, high performance with minimized catalyst loading. J Mater Chem 2017;5:15021–5.
- [6] Edwards PP, Kuznetsov VL, David WIF, Brandon NP. Hydrogen and fuel cells: towards a sustainable energy future. Energy Pol 2008;36:4356–62.
- [7] Gür TM. Comprehensive review of methane conversion in solid oxide fuel cells: prospects for efficient electricity generation from natural gas. Prog Energy Combust Sci 2016;54:1–64.
- [8] Sun C, Hui R, Roller J. Cathode materials for solid oxide fuel cells: a review. J Solid State Electrochem 2010;14:1125–44.
- [9] Badwal SPS, Giddey S, Munnings C, Kulkarni A. Review of progress in high temperature solid oxide fuel cells. J Aust Ceram Soc 2014;50:23—37.
- [10] Vostakola MF, Horri BA. Progress in material development for low-temperature solid oxide fuel cells: A review. Energies 2021;14(5):1280.
- [11] Gao Z, V Mogni L, Miller EC, Railsback JG, Barnett SA. A perspective on low-temperature solid oxide fuel cells. Energy Environ Sci 2016;9:1602–44.
- [12] Boukamp BA. Electrochemical impedance spectroscopy in solid state ionics: recent advances. Solid State Ionics 2004;169:65–73.
- [13] Nielsen J, Hjelm J. Impedance of SOFC electrodes: a review and a comprehensive case study on the impedance of LSM:YSZ cathodes. Electrochim Acta 2014;115:31–45.
- [14] Huang Q-A, Liu M, Liu M. Impedance spectroscopy study of an SDC-based SOFC with high open circuit voltage. Electrochim Acta 2015;177:227—36.
- [15] Wan TH, Saccoccio M, Chen C, Ciucci F. Influence of the discretization methods on the distribution of relaxation times deconvolution: implementing radial basis functions with DRTtools. Electrochim Acta 2015;184:483—99.
- [16] Ivers-tiffée E, Weber A. Evaluation of electrochemical impedance spectra by the distribution of relaxation times. J. Ceram. Soc. Japan 2017;125:193—201.
- [17] Kube A, Strunz W, Wagner N, Andreas Friedrich K. Evaluation of electrochemical impedance spectra of batteries (Li-air/Zn-air) for aqueous electrolytes. Electrochim Acta 2021;396:139261.
- [18] Schichlein H, Müller AC, Voigts M, Krügel A, Ivers-Tiffée E. Deconvolution of electrochemical impedance spectra for the identification of electrode reaction mechanisms in solid oxide fuel cells. J Appl Electrochem 2002;32:875—82.
- [19] Dierickx S, Weber A, Ivers-Tiffée E. How the distribution of relaxation times enhances complex equivalent circuit models for fuel cells. Electrochim Acta 2020;355:136764.
- [20] Shi N, Su F, Huan D, Xie Y, Lin J, Tan W, Peng R, Xia C, Chen C, Lu Y. Performance and DRT analysis of P-SOFCs fabricated using new phase inversion combined tape casting technology. J Mater Chem 2017;5:19664–71.
- [21] Kornely M, Menzler NH, Weber A, Ivers-Tiffée E. Degradation of a high performance SOFC cathode by Cr-poisoning at OCV-conditions. Fuel Cell 2013;13:506—10.
- [22] Wang CC, Darvish S, Chen K, Hou B, Zhang Q, Tan Z, et al. Combined Cr and S poisoning of $La_{0.8}Sr_{0.2}MnO_{3-\delta}$ (LSM) cathode of solid oxide fuel cells. Electrochim Acta 2019;312:202–12.
- [23] Wang H, Sumi H, Barnett SA. Effect of high-temperature ageing on (La,Sr)(Co,Fe)O_{3-δ} cathodes in microtubular solid oxide fuel cells. Solid State Ionics 2018;323:85–91.

- [24] Chen K, Li N, Ai N, Cheng Y, Rickard WDA, Jiang SP. Polarization-induced interface and Sr segregation of in situ assembled $La_{0.6}Sr_{0.4}Co_{0.2}Fe_{0.8}O_{3-\delta}$ electrodes on $Y_2O_3-ZrO_2$ electrolyte of solid oxide fuel cells. ACS Appl Mater Interfaces 2016;8:31729–37.
- [25] Mark BT, Orazem E. Electrochemical impedance spectroscopy. 2nd ed. Wiley; 2017.
- [26] Jiang SP. Development of lanthanum strontium cobalt ferrite perovskite electrodes of solid oxide fuel cells – a review. Int J Hydrogen Energy 2019;44:7448–93.
- [27] Lane JA, Benson SJ, Waller D, Kilner JA. Oxygen transport in $La_{0.6}Sr_{0.4}Co_{0.2}Fe_{0.8}O_{3-\delta}$. Solid State Ionics 1999;121:201–8.
- [28] Sumi H, Yamaguchi T, Hamamoto K, Suzuki T, Fujishiro Y . High performance of La_{0.6}Sr_{0.4}Co_{0.2}Fe_{0.8}O₃-Ce_{0.9}Gd_{0.1}O_{1.95} nanoparticulate cathode for intermediate temperature microtubular solid oxide fuel cells. J Power Sources 2013;226:354-8.

- [29] Sumi H, Shimada H, Yamaguchi Y, Mizutani Y, Okuyama Y, Amezawa K. Comparison of electrochemical impedance spectra for electrolyte-supported solid oxide fuel cells (SOFCs) and protonic ceramic fuel cells (PCFCs). Sci Rep 2021;11:10622.
- [30] Lim D-K, Kim J-H, Chavan AU, Lee T-R, Yoo Y-S, Song S-J. Performance of proton-conducting ceramic-electrolyte fuel cell with BZCY40 electrolyte and BSCF5582 cathode. Geram Int 2016;42:3776–85.
- [31] Byron Bird ENLR, Stewart Warren E. Transport phenomena. Wiley, Revised 2nd.; 2009.
- [32] Sumi H, Yamaguchi T, Hamamoto K, Suzuki T, Fujishiro Y, Matsui T, Eguchi K. AC impedance characteristics for anodesupported microtubular solid oxide fuel cells. Electrochim Acta 2012;67:159–65.
- [33] Osinkin DA. Detailed analysis of electrochemical behavior of high-performance solid oxide fuel cell using DRT technique. J Power Sources 2022;527:231120.